CENOZOIC CLIMATE

Global and regional temperature change over the past 4.5 million years

Peter U. Clark[1,2]*†, Jeremy D. Shakun[3]†, Yair Rosenthal[4,5], Peter Köhler[6], Patrick J. Bartlein[7]

Much of our understanding of Cenozoic climate is based on the record of $\delta^{18}O$ measured in benthic foraminifera. However, this measurement reflects a combined signal of global temperature and sea level, thus preventing a clear understanding of the interactions and feedbacks of the climate system in causing global temperature change. Our new reconstruction of temperature change over the past 4.5 million years includes two phases of long-term cooling, with the second phase of accelerated cooling during the Middle Pleistocene Transition (1.5 to 0.9 million years ago) being accompanied by a transition from dominant 41,000-year low-amplitude periodicity to dominant 100,000-year high-amplitude periodicity. Changes in the rates of long-term cooling and variability are consistent with changes in the carbon cycle driven initially by geologic processes, followed by additional changes in the Southern Ocean carbon cycle.

Much of our understanding of Cenozoic climate and sea level change is based on the record of $\delta^{18}O$ measured in benthic foraminifera ($\delta^{18}O_b$) (*1*–*3*) (Fig. 1A), which reflects some combination of local water temperature and the $\delta^{18}O$ of seawater ($\delta^{18}O_{sw}$), with the latter largely recording land-ice volume and thus sea level. Over the past 4.5 million years (Myr), this record suggests that Earth experienced long-term cooling and there were several large transitions in climate and ice sheet variability. These included the intensification of Northern Hemisphere (NH) glaciation between 3.0 and 2.5 million years ago (Ma) (*4*) and a switch from lower-amplitude, higher-frequency [41 thousand years (kyr)] variability to higher-amplitude, lower-frequency (~100-kyr) variability during the Middle Pleistocene Transition (MPT) ~1 Ma (Fig. 1A) (*5*, *6*). The $\delta^{18}O_b$ record has also been key in establishing that the periodic growth and decay of ice sheets during the Pleistocene were paced by changes in seasonal and latitudinal changes in insolation from Earth's orbital variations on 10^4- to 10^5-year timescales (*7*–*9*). Interactions and feedbacks between ice sheets and the carbon cycle, land cover, ocean circulation, and other components of the Earth system then transferred the seasonal and latitudinal changes in insolation forcing into global surface temperature changes of 4° to 6°C (*10*) and sea level fluctuations of as much as 135 m (*11*).

Understanding this evolution of Pliocene and Pleistocene long-term climate and its variability in response to orbital forcing remains a substantial challenge in climate dynamics (*8*, *9*, *12*, *13*). For example, both the intensification of NH glaciation and the MPT occurred in the absence of any change in orbital forcing (*5*, *14*). Moreover, early Pleistocene climate and sea level variability was dominated by 41-kyr obliquity cycles despite summer insolation being dominated by the 23-kyr precessional frequency (*12*, *15*), and the dominant post-MPT ~100-kyr variability occurred despite there being virtually no forcing emanating from the 100-kyr eccentricity cycle (*9*).

This challenge partly hinges on uncertainties in temperature and sea level reconstructions that prevent a more complete explanation of the mechanisms responsible for ice sheet–climate interactions and their joint responses to orbital forcing that led to these long-term changes. For example, the relative contribution of temperature and $\delta^{18}O_{sw}$ to the $\delta^{18}O_b$ record has long been debated (*16*–*18*), and it is likely that their relationship is nonstationary (*19*–*21*). Individual sea surface temperature (SST) records do not record the global average changes that are required to assess hypotheses invoking CO_2 changes for the onset and intensification of NH glaciation (*13*) or the cause of the MPT (*22*) or to validate climate-model simulations (*23*, *24*). Finally, there have been few systematic assessments of SST records from different regions of the world's ocean for orbital-scale changes (*25*) or of changes in SST gradients beyond differencing individual records that may have local biases (*26*).

Here, we address these issues by stacking published SST records that span some to all of the past 4.5 Myr to reconstruct global and regional temperature differences (ΔSST) from the late Holocene (i.e., 0°C at 0 ka). We then use a scaling relation established by climate models to derive changes in global mean surface temperature (ΔGMST) from our global ΔSST reconstruction. Our reconstructions establish a new framework for understanding global temperature evolution that is independent of the mixed-signal $\delta^{18}O_b$ record, as well as for constraining climate sensitivity that reflects the slow feedbacks that will unfold over the coming centuries to millennia in response to anthropogenic forcing (*27*). Our regional ΔSST stacks provide insights into regional departures from the global SST signal, changes in zonal and meridional SST gradients that were important in atmospheric circulation (*26*, *28*), and possibly climate sensitivity through the pattern effect (*29*, *30*).

Global SST change

We used 128 published SST records based on alkenone (n = 69), Mg/Ca (n = 42), and faunal (n = 17) proxies that span from 69°N to 56°S (figs. S1 and S2 and table S1). There can be disagreement between alkenones and Mg/Ca proxies, particularly for the long-term trends in the western Pacific warm pool (*31*–*33*), but new clumped-isotope data tend to support the Mg/Ca reconstructions (*34*). We generated two global ΔSST stacks: one averaging unweighted all records (ΔSST_{all}) (<400-kyr resolution) and a second with records that have <20-kyr resolution weighted by 15° latitude bands ($\Delta SST_{hi\text{-}res}$) (Fig. 1B and fig. S3), which, with an average 2- to 4-kyr resolution for the past 3 Myr, allows us to assess orbital-scale (10^4 to 10^5 year) variability (fig. S4A) (see the supplementary materials, sections 1 and 2). Despite the $\Delta SST_{hi\text{-}res}$ stack having two to three times fewer records than the ΔSST_{all} stack (fig. S2H), 400-kyr averages of the two stacks are the same (within 1 σ uncertainties) for most of the past 4.5 Myr (fig. S3A). We also determined that the stacking process caused only a small signal loss before 1 Ma due to age misalignments. We did find that the variability of our $\Delta SST_{hi\text{-}res}$ stack was ~0.5° ± 0.1°C less than the average variability of individual records used in the stack (fig. S5, A and B). This signal reduction is expected with a large-scale mean due to cancellation of proxy and local climate noise in individual records, but additional factors such as proxy differences and age uncertainties in the $\delta^{18}O_b$ records used to align our records may result in cancelation of climate signals. We thus conclude that stacking has caused at most a ~0.5° ± 0.1°C reduction in the variability in our ΔSST stack.

Our $\Delta SST_{hi\text{-}res}$ reconstruction suggests that average global ΔSSTs were +2.6° ± 0.9°C (1σ) at 4.5 Ma, gradually increased to +2.9° ± 0.9°C at 4 Ma, and then began a two-phase cooling trend until 0.8 Ma, when they stabilized at −2.1° ± 0.4°C over the remainder of the Pleistocene (Fig. 1C). During the first cooling phase, average global ΔSSTs decreased to +1.8° ± 0.5°C during the late-Pliocene KM5c interglaciation (3.195 to 3.215 Ma) and the

[1]College of Earth, Ocean, and Atmospheric Sciences, Oregon State University, Corvallis, OR 97331, USA. [2]School of Geography and Environmental Sciences, University of Ulster, Coleraine BT52 1SA, Northern Ireland, UK. [3]Department of Earth and Environmental Sciences, Boston College, Chestnut Hill, MA 02467, USA. [4]Department of Marine and Coastal Science, Rutgers The State University, New Brunswick, NJ 08901, USA. [5]Department of Earth and Planetary Sciences, Rutgers The State University, New Brunswick, NJ 08901, USA. [6]Alfred-Wegener-Institut Helmholtz-Zentrum für Polar- und Meeresforschung, 27570 Bremerhaven, Germany. [7]Department of Geography, University of Oregon, Eugene, OR 97403, USA.
*Corresponding author. Email: clarkp@onid.orst.edu
†These authors contributed equally to this work.

mid-Piacenzian Stage (3.025 to 3.264 Ma), in agreement with independent reconstructions for these intervals [+2.3°C (*35*), +2.2° ± 1.1°C (*36*)] (fig. S7A). A gradual increase in variability began ~4 Ma, followed by a rapid increase beginning at ~1.5 Ma (figs. S5D and S6E). There was no significant change in the rate of cooling nor in variability during the period of intensification of NH glaciation between 3 and 2.5 Ma, as opposed to an acceleration in cooling and increase in variability during the MPT that marks the second phase of cooling (Fig. 1C).

There is generally good agreement between variability in our ΔSST reconstruction and other proxy-based reconstructions (*11*, *37*, *38*) (fig. S8, A, C, and D), including one reconstruction for the past ~135 kyr (fig. S8E) (*39*) that is based on a significantly larger number of faunal records and a larger latitudinal range than ours. A reconstruction based on a climate model of intermediate complexity (*24*) (fig. S8B) underestimates the amount of cooling shown by our stack over the past 3 Myr, as well as during glaciations over the past 0.8 Myr, suggesting that model forcing or sensitivity may be too small.

Our ΔSST reconstruction for the Last Glacial Maximum (LGM, 26 to 19 ka), −3.3° ± 0.4°C, agrees within uncertainty with a reconstruction using only geochemical proxies, −2.9°C, −3.0° to −2.7°C, 95% confidence interval (CI) (Fig. 1B), which is based on about nine times as many records as ours with a larger latitudinal range and with their estimate from a global climate model with data assimilation (−3.1°C; −3.4° to −2.9°C, 95% CI) (*40*). However, our reconstruction is substantially cooler than another recent proxy-based estimate (−1.7° ± 0.1°C) (*41*) that is derived from the MARGO (*42*) dataset (−1.9° ± 1.8°C), which, by including estimates from microfossil transfer functions that may have no-analog biases (*43*), likely explains the smaller LGM cooling. Our reconstruction is also colder than one derived from data assimilation techniques (−2.2°C, −3.2° to −1.2°C, 95% CI) (*44*) that uses a combination of MARGO data and data from (*40*). We further address differences in LGM ΔGMST temperature reconstructions below.

Global mean surface temperature change

We found that the spatial coverage of the SST data are adequate to reconstruct GMST by sampling two spatially intensive records, the instrumental record of the past 150 years (*45*) and the TraCE-21 global climate model simulation of the past 22,000 years (*46*), at the locations of the sites that provided reconstructions over 1-Myr time spans (fig. S1) (see the supplementary materials, section 2, and fig. S9). We then used results from climate model experiments to scale global ΔSSTs to ΔGMST (see the supplementary materials, section 3, and fig. S10). Our scaling factors for climates colder than preindustrial (PI) are in good agreement with scaling factors derived from simulated LGM ΔSSTs and ΔGMSTs (fig. S10) (*40*, *47*, *48*) that were used to reconstruct changes in ΔGMST from a ΔSST stack for the last deglaciation (*10*) and the past 2 Myr (*48*).

Being derived from our $\Delta SST_{hi\text{-}res}$ stack, our $\Delta GMST_{hi\text{-}res}$ stack exhibits similar trends and variability, albeit with different rates and amplitudes, respectively (Fig. 1D). Average ΔGMSTs were +3.7° ± 1.4°C at 4.5 Ma, gradually warmed to +4.0° ± 1.4°C at 4 Ma, and then began the first phase of gradual cooling (−0.0015°C kyr^{-1}), with a decrease to +2.9° ± 0.8°C during the KM5c interglaciation, in agreement with the Pliocene Model Intercomparison Project 2 (PLIOMIP2) ensemble using atmospheric CO_2 of 400 ppm (+3.2° ± 1.7°C) (*49*) (Fig. 1D and fig. S7B). Average ΔGMST continued to decrease steadily, whereas variability continued to increase gradually through the early Pleistocene, again showing no acceleration in long-term cooling nor in variability during NH ice sheet intensification. The second phase of cooling began ~1.5 Ma, when long-term cooling rates tripled to −0.005°C kyr^{-1} and variability nearly doubled during the MPT (Fig. 1E). Average ΔGMSTs then stabilized by 0.8 Ma at −3.8° ± 0.7°C, with a total long-term average cooling of 7.8° ± 1.6°C since 4 Ma (Fig. 1D). These contrasting GMST responses to two intervals of NH ice sheet expansion suggested by the $\delta^{18}O_b$ record (Fig. 1A) suggest either a limited efficacy of ice sheet forcing (*50*, *51*), with MPT cooling occurring in response to some other forcing, or an increase in ice sheet efficacy during the MPT.

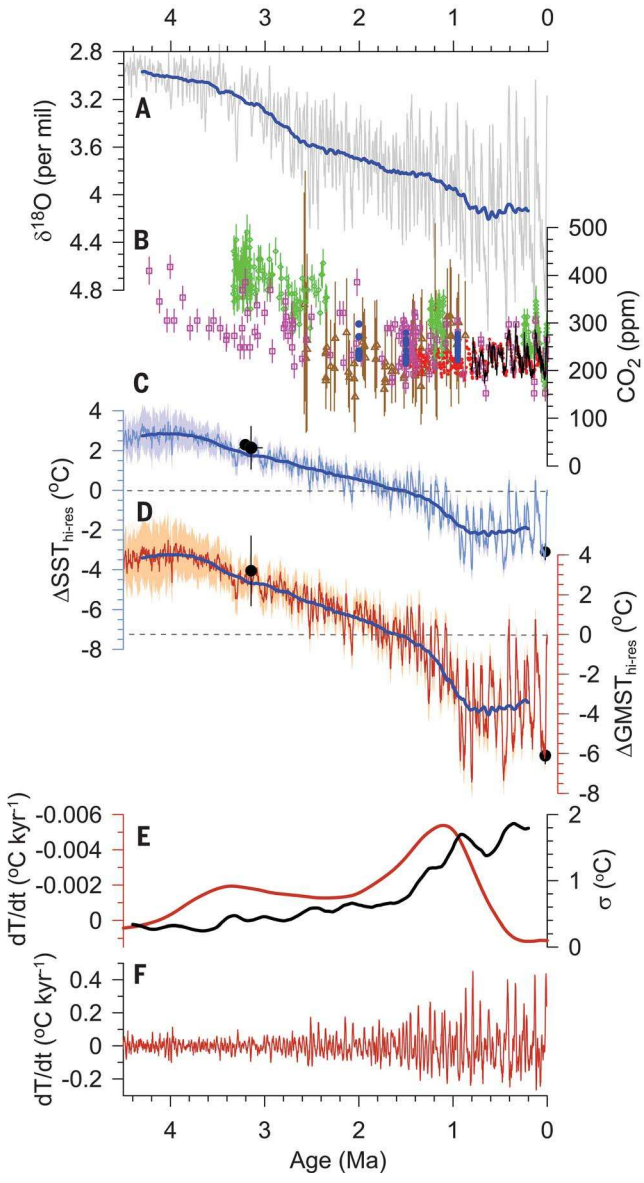

Fig. 1. Global temperature changes over the past 4.5 Myr. (**A**) The $\delta^{18}O_b$ record is shown in gray (*2*), with 400-kyr running average in blue. (**B**) Proxy and ice-core CO_2 data. Magenta and green symbols are harmonized $\delta^{11}B$ values on planktonic foraminifera *T. sacculifer* and *G. ruber*, respectively (*64*). Other CO_2 data are based on measurements on soil carbonate (brown symbols) (*89*), $\delta^{13}C$ of leaf wax (red symbols) (*90*), and ice cores [blue symbols (*91*) and black line (*92*)]. (**C**) Global SST change ($\Delta SST_{hi\text{-}res}$) (light blue with 1σ uncertainty; long-term average in dark blue) referenced to PI. Black circles represent ΔSSTs for the Pliocene KM5c interglaciation (*35*), the mid-Piacenzian Stage (*36*), and the LGM (*40*). (**D**) $\Delta GMST_{hi\text{-}res}$ (brick red with 1σ uncertainty; long-term average in blue) referenced to PI. Black circles represent ΔGMSTs for the Pliocene KM5c interglaciation (*49*) and for the LGM (*40*). (**E**) Rate of change of ΔGMST (brick-red line, spline fit) and standard deviation (σ, black line, 200-kyr centered) of ΔGMST. (**F**) Rate of change of ΔGMST (12-kyr running average).

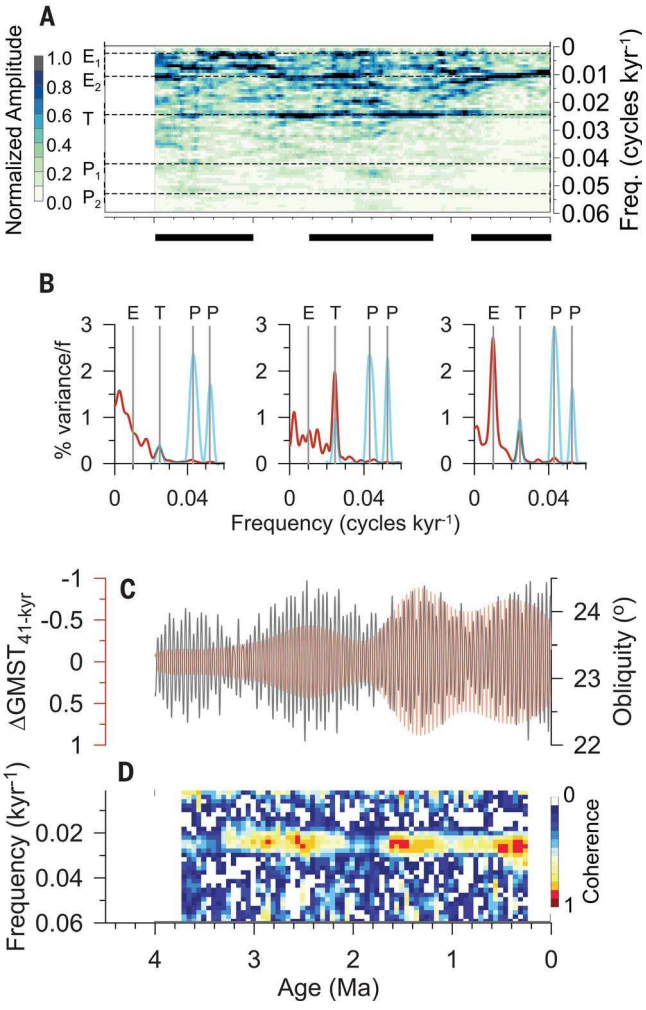

Fig. 2. Changes in variance spectrum of global temperature. (**A**) Evolutionary spectrum of ΔGMST plotted as normalized amplitudes. The dominant periods in insolation variations at orbital periods are indicated by horizontal lines: eccentricity (E_1) = 400 kyr, E_2 = 96 kyr, obliquity (T) = 41 kyr, precession (P_1) = 23 kyr, and P_2 = 19 kyr. (**B**) Spectral density of ΔGMST and insolation for three periods corresponding to horizontal black bars shown under the *x* axis of (A) (3 to 4 Ma, 1.2 to 2.5 Ma, and 0 to 0.8 Ma). (**C**) Obliquity (black line) and filtered ΔGMST using a 41-kyr filter (brick-red line). (**D**) Coherence between 41-kyr filtered ΔGMST and obliquity.

Our reconstruction exhibits up to 3°C more cooling over the past 4.5 Myr and a greater amplitude of change over the past 800 kyr than simulated by intermediate-complexity climate models (fig. S11, A, B, and D) (*23*, *24*, *52*), again suggesting that model forcing or sensitivity is too low. Our reconstruction similarly shows greater long-term cooling and differences in amplitude than one derived from a $\delta^{18}O_b$ stack (fig. S11C) (*3*, *53*), which we infer reflects uncertainties in their assumptions used to derive ΔGMST. Our reconstruction also differs from a proxy-based ΔGMST reconstruction developed for the past 2 Myr, which inferred that GMST cooling had stabilized at the beginning of the MPT (*48*) as opposed to at the end of the MPT, which was seen in our stack (fig. S11E). We attribute these differences to the 2-Myr reconstruction being based on many fewer records than ours, especially for >0.5 Ma (fig. S2H).

Our ΔGMST reconstruction for the LGM (−6.0° ± 0.6°C) is in good agreement with several other recent proxy reconstructions that were also derived by scaling global SSTs similar to our approach (*10*, *40*, *48*) and with an estimate derived by using climate models to scale a reconstruction of mean ocean temperature to GMST change (*54*). References (*40*) and (*10*) also estimated LGM GMST by using data assimilation with an ensemble prior from a single climate model, with the difference between the two (−6.1°C versus −6.8°C) reflecting differences in model priors, data distribution, and other methodologies. Reference (*44*) attributed the extent of cooling suggested by these data assimilation studies to the use of one single model prior that simulates a relatively cold LGM state, although their assimilated value falls entirely within the error bounds of their data-only ΔGMST (*40*). Using a model prior ensemble that includes a number of models with a wider range of LGM temperatures that on average simulate less cooling than the prior in (*40*) indeed finds less cooling (−4.5° ± 0.9°C) (*44*). This result, however, may reflect in part the inclusion of warm-biased MARGO SST data as well as the warmer prior ensemble nudging the data to warmer LGM temperatures.

We next examined the spectral characteristics of our ΔGMST reconstruction. A small concentration of variance in the obliquity band during the Pliocene markedly increased at ~2.6 Ma, dominated until ~1.2 Ma, and persisted throughout the remainder of the Pleistocene (Fig. 2, A and B). The 41-kyr ΔGMST signal over the past 4 Myr exhibits amplitude modulation corresponding to a 1.2-Myr obliquity modulation (Fig. 2C), with lowest coherence between the two occurring during their corresponding low-amplitude intervals (nodes) (Fig. 2D). We found that a small fraction of precessional variance appeared between 2 and 1.5 Ma (Fig. 2A), which is centered on a low-amplitude node at 1.8 Ma (Fig. 2, C and D). This node also coincides with an interval of increased precessional forcing from eccentricity modulation (*55*), suggesting that the appearance of the precessional signal reflects a combination of diminished obliquity forcing and enhanced precessional forcing.

A strong increase in ΔGMST variability occurred ~1.5 Ma, when long-term average ΔGMST first decreased below PI and reached its current level at ~0.8 Ma (Fig. 1, D and E). The emergence of low-frequency (~100-kyr) variability began ~1.2 Ma and dominated throughout the past ~0.8 Myr (Fig. 2, A and B), although it was not strictly centered on the eccentricity frequency bands throughout most of this interval. The overall increase in variability ~1.5 Ma, the emergence of the low-frequency component ~1.2 Ma, and peak rates of long-term cooling between 1.2 and 0.8 Ma is the temperature expression of the MPT.

Regional SST change

To gain insight into regional SST contributions to global temperature change, we parsed SST records in various ways that capture important aspects of regional ΔSST trends, gradients, and variability (Fig. 3, figs. S12 and S13, and table S2). These results indicated that global cooling was occurring ~4 Ma in all ocean areas except the Indo-Pacific warm pool (IPWP), with greatest rates of cooling in the NH extratropics and subtropical upwelling regions (*26*) (Fig. 3 and fig. S14). None of the regional stacks showed an acceleration in cooling during intensification of NH glaciation between 3 and 2.5 Ma (fig. S15), consistent with the limited geographic scope of ice sheet forcing identified by climate models (*56*). By contrast, other than the IPWP, all regions of the world's oceans showed an increase in the rate of cooling during the MPT (fig. S15). Regional ΔSST then stabilized between 1 and 0.8 Ma (Fig. 3). The consistency of regional trends in ΔSST, which showed two phases of cooling, with the greatest rates of cooling occurring at higher latitudes and no clear expression of ice sheet forcing, provides a clear fingerprint of CO_2 forcing of long-term global temperature change over the past 4 Myr (*52*, *56*).

The late-Pliocene IPWP-eastern tropical Pacific zonal temperature gradient was 0.5° to 1.5°C, ~2°C less than the late-Pleistocene average (Fig. 3I). Extratropical hemispheric meridional SST gradients were also substantially reduced (*28*) (Fig. 3, H and M), supporting the notion of a greatly expanded tropical warm pool with a deeper equatorial thermocline (*57*) during the Pliocene (*26*, *31*, *58*). Zonal and meridional gradients then began to increase ~2 Ma and reached their present values by ~1 Ma (Fig. 3, H and I). Finally, most regional stacks show the same evolution of frequency spectrum as in the global stack, including a 41-kyr periodicity that persisted since the start of the Pleistocene and the onset of ~100-kyr periodicity at ~1.2 Ma associated with the MPT (Fig. 3, D to F, and fig. S16).

We found good agreement between our Southern Hemisphere (SH) extratropical ΔSST reconstruction and a reconstruction of South Atlantic and Indian Ocean SSTs derived from the 720-kyr Dome F (DF) Antarctic ice core (fig. S17, A and D). Our regional ΔSST (fig. S17B) and ΔGMST (fig. S17C) reconstructions also share the same temporal variability in temperature derived from the 800-kyr EPICA Dome C (EDC) ice core (fig. S17B), with the latter having a greater amplitude of change (fig. S17D). A recent assessment, however, suggested that LGM cooling over East Antarctica may be significantly less than previously inferred from ice cores (*59*), with the newly inferred cooling at the EDC site (-4.3° ± 1.5°C) being comparable to cooling in our SH extratropical ΔSST reconstruction (–3.8° ± 0.5°C), suggesting less Antarctic amplification. The agreement between these records over the periods of overlap suggests that our SH extratropical ΔSST reconstruction may serve as a template of variability for any forthcoming >0.8-Ma Antarctic ice-core temperature reconstructions (*60*).

CO_2 forcing of late Pliocene-Pleistocene temperature change

Our reconstructed global cooling over the past 4 Myr is consistent with the long-term cooling trend that began ~15 Ma after the Miocene Climatic Optimum (*61*, *62*). This post-15 Ma cooling is commonly attributed to decreasing atmospheric CO_2 (*61*, *63*), which, on these geologic timescales, results from an imbalance between tectonic outgassing and chemical weathering of silicate rocks with an additional contribution from the SST-CO_2 feedback (*64*). The similar gradual rates of cooling of the previous 11 Myr (*61*) to those from 4 to 1.5 Ma indicate that this first phase of cooling in our reconstruction could have occurred as a straightforward continuation of this CO_2 forcing. However, reference (*61*) found that the decreasing trend in mid–ocean ridge outgassing rates stabilized ~6 Ma, which requires additional increases in silicate weathering to continue CO_2 drawdown and the rate of cooling after 6 Ma. Indeed, reference (*65*) found that a similar decrease in mid–ocean ridge outgassing as in (*61*) was accompanied by a greater increase in subduction outgassing, leading to a net increase in tectonic CO_2 emissions over the past 15 Myr that reinforces the need for a concomitant increase in silicate weathering. Several

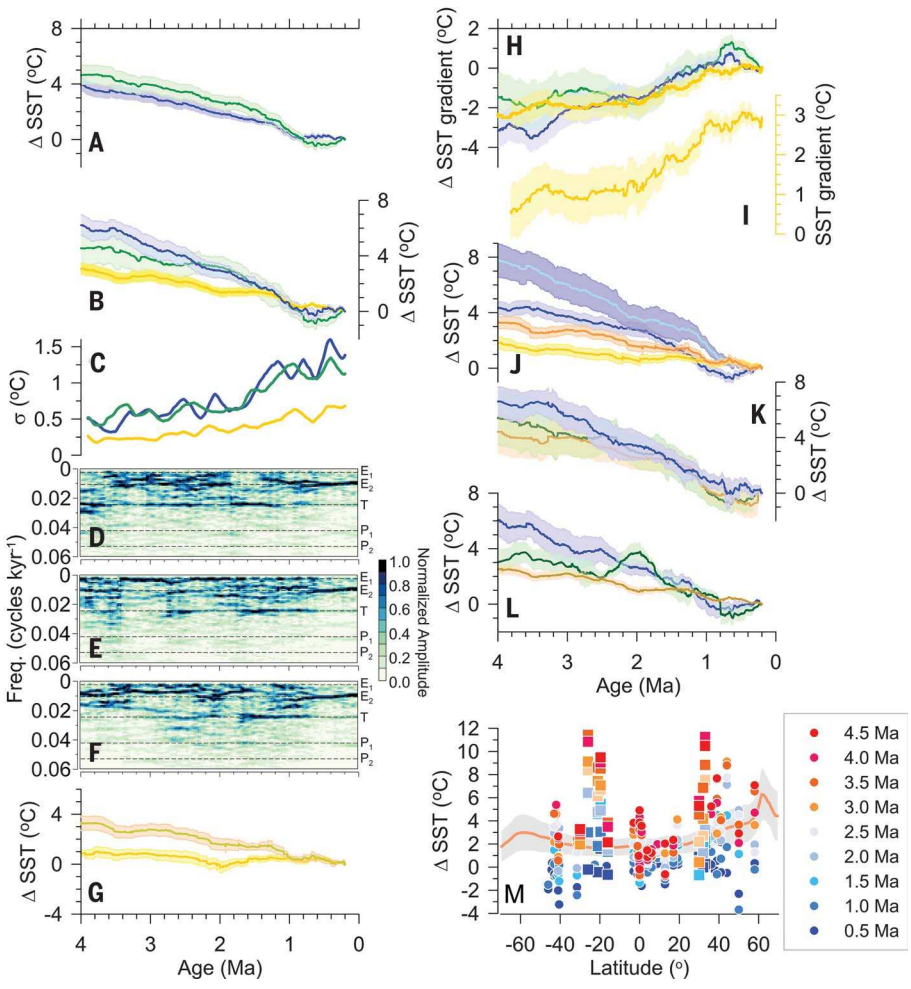

Fig. 3. Regional ΔSST changes over the past 4 Myr. Regional ΔSST stacks shown as 400-kyr running averages and shifted by the 0- to 400-ka mean. (**A**) NH (blue) and SH (green) shown with 1σ uncertainty. (**B**) Northern extratropics (blue), tropics (yellow), and southern extratropics (green) with 1σ uncertainty. (**C**) SD (σ) of high-resolution (>20-kyr) northern extratropical (blue), tropical (yellow), and southern extratropical (green) ΔSST stacks. (**D**) Evolutionary spectrum of northern extratropical ΔSST stack plotted as normalized amplitudes. The dominant periods in insolation variations at orbital periods are indicated by horizontal lines: E_1 = 400 kyr, E_2 = 96 kyr, T = 41 kyr, P_1 = 23 kyr, and P_2 = 19 kyr. (**E**) Evolutionary spectrum of tropical ΔSST stack plotted as normalized amplitudes. The dominant periods in insolation variations at orbital periods are indicated by horizontal lines: E_1 = 400 kyr, E_2 = 96 kyr, T = 41 kyr, P_1 = 23 kyr, and P_2 = 19 kyr. (**F**) Evolutionary spectrum of southern extratropical ΔSST stack plotted as normalized amplitudes. The dominant periods in insolation variations at orbital periods are indicated by horizontal lines: E_1 = 400 kyr, E_2 = 96 kyr, T = 41 kyr, P_1 = 23 kyr, and P_2 = 19 kyr. (**G**) IPWP (yellow) and eastern tropical Pacific (ETP) (light green) ΔSST stacks with 1σ uncertainties. (**H**) ΔSST gradients with 1σ uncertainties for NH extratropics minus tropics (blue), SH extratropics minus tropics (green), and IPWP minus ETP (yellow). (**I**) IPWP minus ETP SST gradient (with 1σ uncertainty); 28.3°C was added to the IPWP ΔSST stack and 25.4°C to the ETP ΔSST stack, with these values representing the average SSTs for period 1901 to 1930 at the core sites in the two regions. (**J**) ΔSST stacks with 1σ uncertainties for regions identified by Fedorov *et al.* (*26*): subtropical coastal upwelling (light blue), mid-high latitudes (blue), warm pool (deep yellow), and equatorial upwelling (light orange). (**K**) ΔSST stacks with 1σ uncertainties for the Atlantic basin: North Atlantic (blue), tropical Atlantic (gold), and South Atlantic (green). (**L**) ΔSST stacks with 1σ uncertainties for the Pacific basin: North Pacific (blue), tropical Pacific (gold), and South Pacific (green). (**M**) ΔSSTs for individual site records by latitude binned into 0.5-Myr intervals and distinguished by sites from subtropical coastal upwelling regions (squares) (*26*) versus all other areas (circles). Also shown are the zonal mean ΔSSTs (orange line with 1σ uncertainty in gray area) from the PLIOMIP2 model ensemble for the KM5c interglaciation (3.195 to 3.215 Ma) (*49*).

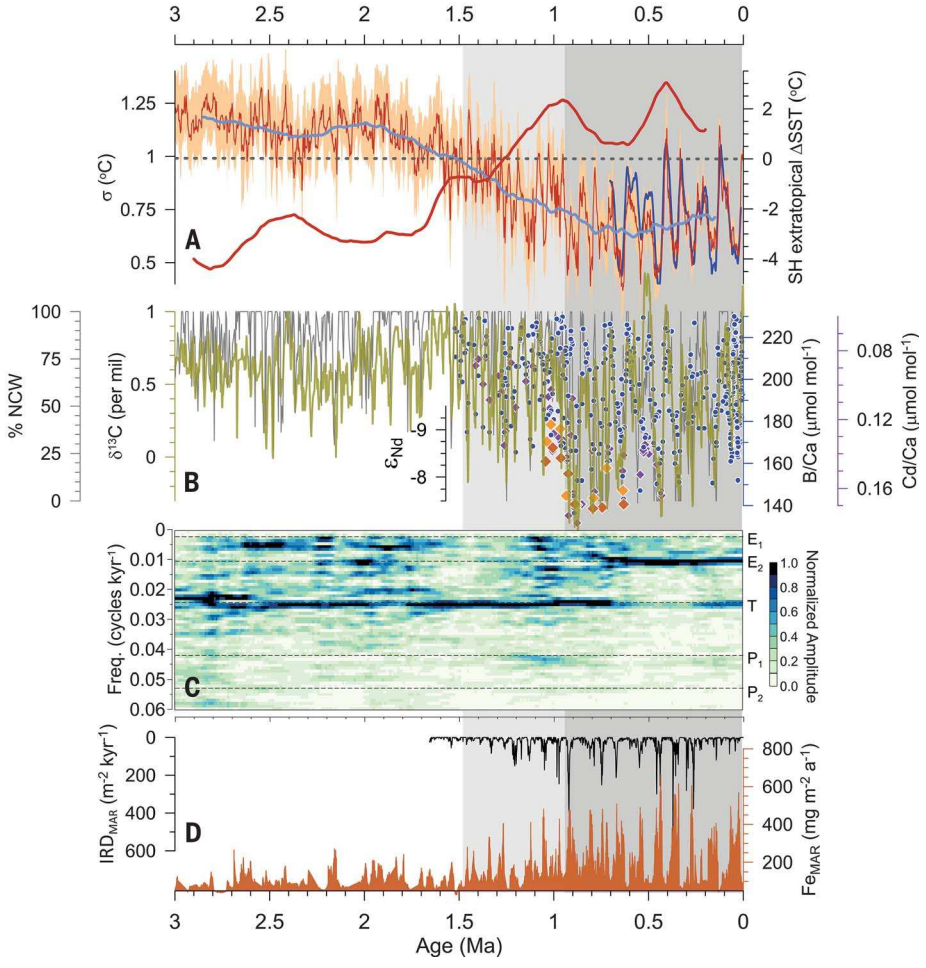

Fig. 4. Assessing the origin of the MPT. (**A**) SH extratropical ΔSST stack (brick-red line with 1σ uncertainty and 201-kyr running average in light blue) and SST reconstruction for Southern Ocean derived from deuterium excess from the Dome Fuji Antarctic ice core (blue = 25-kyr running average) (*93*). SD (σ) of the ΔSST stack is shown by a thick brick-red line. (**B**) $\delta^{13}C$ stack of mid-to-deep Atlantic cores (green) (*83*), % northern component water (NCW) (gray) (*94*), ε_{Nd} data from South Atlantic sites ODP 1088 and 1090 (*84*), and Cd/Ca and B/Ca data from North Atlantic cores CHN82-24-23PC and DSDP 607 (*85*, *86*) and South Atlantic site ODP 1267 (*87*). (**C**) Evolutionary spectra of $\delta^{13}C$ stack shown in (B) plotted as normalized amplitudes. The dominant periods in insolation variations at orbital periods are indicated by horizontal lines: E_1 = 400 kyr, E_2 = 96 kyr, T = 41 kyr, P_1 = 23 kyr, and P_2 = 19 kyr. (**D**) Ice-rafted debris from South Atlantic sites MD02-2588 and IODP site 1475 (black line) (*77*) and record of iron flux to the South Atlantic from South Atlantic site ODP 1090 (*76*).

lines of evidence indicate that the uplift of the Southeast Asia islands beginning ~15 Ma helped meet this requirement by exposing ophiolitic rocks to chemical weathering, with the largest increase of island exposure and chemical weathering starting ~4 Ma (*63*, *66*). Uncertainties in CO_2 proxies over the past 15 Myr, however, prevent us from assessing whether the carbon budget based on these published source and sink terms is closed and what trajectory decreasing CO_2 followed (*64*, *67*) (Fig. 1B).

Some studies suggest that changes in the Southern Ocean carbon cycle and associated atmospheric CO_2 variability contributed to the increase in amplitude and decrease in frequency of ΔGMST change across the MPT (*68*, *69*), which are two of the three hallmarks of the temperature expression of the MPT. Here, we build on this hypothesis by arguing that changes in the Southern Ocean carbon cycle also caused the third hallmark, the second phase of accelerated long-term cooling in ΔGMST. In this hypothesis, the first phase of gradual cooling initiated the MPT at ~1.5 Ma, when average SH extratropical ΔSSTs (derived here from sites between 30° and 45°S) first decreased below 0°C (lower than at PI) (Fig. 4A). From 3 to 1.5 Ma, SH extratropical ΔSSTs spent ~90% of the time above PI, but then spent increasingly more time below PI (~85% during the MPT, ~95% since 0.9 Ma). Such cooling initiated two simultaneous changes in sea ice: an increase in its long-term average extent (*70*) and an increase in its sensitivity to the dominant obliquity forcing at these high latitudes, thus increasing the variability in its extent. Models have identified the role that increased Antarctic sea ice plays in enhancing formation of salty and dense Antarctic Bottom Water (AABW) and increasing carbon storage in the stratified deep ocean (*68*, *71*–*75*). This indicates that once the 0°C PI threshold in SH extratropical ΔSSTs was crossed, sea ice expansion, through its impact on the Southern Ocean, caused greater carbon sequestration, thus increasing the rate of the ongoing long-term decrease in CO_2 and ΔGMST associated with the long-term carbon cycle. At the same time, an increase in sea ice variability in response to obliquity forcing increased carbon storage during glaciations, thus increasing orbital-scale variability of CO_2 and temperature. Cooling of the SH also led to an increase in aridity and associated iron flux to the Southern Ocean during glaciations (Fig. 4D), thus further contributing to ocean sequestration of CO_2 by iron fertilization (*76*). Greater cooling of SH extratropical SSTs during glaciations also led to more northerly transport of icebergs (*77*) (Fig. 4D), which, together with enhanced sea ice export and melting, led to greater stratification of surface waters over the Southern Ocean (*78*).

Long-term average SH extratropical ΔSSTs further decreased to and then remained below −2°C at 0.9 Ma (Fig. 4A), when their periodicity changed from dominantly 41 to ~100 kyr (Fig. 3F). Under the now-colder temperatures and greater feedback potential, we suggest that this change in frequency resulted from a further increase in sea ice expansion and surface freshening after an interglaciation, thus muting their response to subsequent obliquity forcing. Post-MPT insolation then forced retreat of large NH ice sheets, likely aided by ice sheet instabilities (*79*, *80*) and interactions of millennial- and orbital-scale variations in Earth's climate (*81*). The associated meltwater forcing then caused a decrease in the Atlantic meridional overturning circulation, resulting in warming of the Southern Ocean, retreat of sea ice, and release of CO_2 that terminated each ~100-kyr cycle (*82*).

Deep ocean water masses show changes that are consistent with forcing by the long-term cooling and inferred changes in sea ice and carbon storage. Starting at ~1.5 Ma, there was an increasing frequency of more-negative obliquity-paced $\delta^{13}C$ glacial values recording an increasing influence of AABW at the expense of NADW in the abyssal ocean (Fig. 4B) (*83*). This was followed by a further step-change increase in AABW at 0.9 Ma (*84*) that was accompanied by an increase in nutrients and a decrease in carbonate ion saturation (*85*–*87*) (Fig. 4B) and the first appearance of sustained ~100-kyr periodicity in $\delta^{13}C$ (Fig. 4C).

We thus conclude that the decrease in long-term average Southern Ocean ΔSSTs below PI initiated changes in the Southern Ocean carbon cycle that caused an acceleration in global cooling accompanied by a change from low-amplitude, high-frequency to high-amplitude, low-frequency temperature variability, which resulted in the MPT changes in regional and global temperature through CO_2 forcing. The global expression of these changes would have been amplified by feedbacks associated with an increase in regional ΔSST temperature gradients (Fig. 3), where a CO_2-forced increase in meridional gradients results in a proportional increase in the zonal equatorial Pacific gradient (*28*), with the zonal response tied to cooling of mid-latitude waters that are subducted into the shallow subtropical cells and upwelled in the eastern equatorial Pacific (*88*). At the same time, strengthening of the meridional gradients would have increased coastal upwelling of cold waters in subtropical and equatorial regions (*26*) (Fig. 3), acting as a further feedback on global cooling. Finally, changes in SST gradients and associated patterns of surface warming can change radiative feedbacks such as clouds and lapse rate changes. This dependence of climate feedbacks on evolving patterns of surface warming, which is particularly pronounced in the tropics, can lead to higher equilibrium climate sensitivity under warmer climates (*29*, *30*).

REFERENCES AND NOTES

1. C. Emiliani, *J. Geol.* **63**, 538–578 (1955).
2. L. E. Lisiecki, M. E. Raymo, *Paleoceanography* **20**, 2004PA001071 (2005).
3. T. Westerhold *et al*., *Science* **369**, 1383–1387 (2020).
4. N. J. Shackleton, N. D. Opdyke, *Nature* **270**, 216–219 (1977).
5. N. G. Pisias, T. C. Moore Jr., *Earth Planet. Sci. Lett.* **52**, 450–458 (1981).
6. N. J. Shackleton, N. D. Opdyke, in *GSA Memoirs*, R. M. Cune, J. D. Hays, Eds. (The Geological Society of America, 1976), vol. 145, pp. 449–464.
7. J. D. Hays, J. Imbrie, N. J. Shackleton, *Science* **194**, 1121–1132 (1976).
8. J. Imbrie *et al*., *Paleoceanography* **7**, 701–738 (1992).
9. J. Imbrie *et al*., *Paleoceanography* **8**, 699–735 (1993).
10. M. B. Osman *et al*., *Nature* **599**, 239–244 (2021).
11. J. D. Shakun, D. W. Lea, L. E. Lisiecki, M. E. Raymo, *Earth Planet. Sci. Lett.* **426**, 58–68 (2015).
12. M. E. Raymo, K. Nisancioglu, *Paleoceanography* **18**, 2002PA000791 (2003).
13. M. Vizcaíno, S. Rupper, J. C. H. Chiang, *Paleoceanography* **25**, PA2205 (2010).
14. P. U. Clark *et al*., *Quat. Sci. Rev.* **25**, 3150–3184 (2006).
15. T. D. Herbert, L. C. Peterson, K. T. Lawrence, Z. Liu, *Science* **328**, 1530–1534 (2010).
16. N. J. Shackleton, *Nature* **215**, 15–17 (1967).
17. J. Chappell, N. J. Shackleton, *Nature* **324**, 137–140 (1986).
18. C. Emiliani, *J. Geol.* **74**, 109–124 (1966).
19. C. Waelbroeck *et al*., *Quat. Sci. Rev.* **21**, 295–305 (2002).
20. P. M. Langebroek, A. Paul, M. Schulz, *Paleoceanography* **25**, PA4203 (2010).
21. E. J. Rohling *et al*., *Sci. Adv.* **7**, eabf5326 (2021).
22. C. J. Berends, P. Köhler, L. J. Lourens, R. S. W. van de Wal, *Rev. Geophys.* **59**, e2020RG000727 (2021).
23. P. Köhler, B. de Boer, A. S. von der Heydt, L. B. Stap, R. S. W. van de Wal, *Clim. Past* **11**, 1801–1823 (2015).
24. M. Willeit, A. Ganopolski, R. Calov, V. Brovkin, *Sci. Adv.* **5**, eaav7337 (2019).
25. E. L. McClymont, S. M. Sosdian, A. Rosell-Mele, Y. Rosenthal, *Earth Sci. Rev.* **123**, 173–193 (2013).
26. A. V. Fedorov *et al*., *Nature* **496**, 43–49 (2013).
27. S. C. Sherwood *et al*., *Rev. Geophys.* **58**, RG000678 (2020).
28. A. V. Fedorov, N. J. Burls, K. T. Lawrence, L. C. Peterson, *Nat. Geosci.* **8**, 975–980 (2015).
29. T. Andrews, J. M. Gregory, M. J. Webb, *J. Clim.* **28**, 1630–1648 (2015).
30. K. C. Armour, C. M. Bitz, G. H. Roe, *J. Clim.* **26**, 4518–4534 (2013).
31. A. C. Ravelo, K. T. Lawrence, A. Fedorov, H. L. Ford, *Science* **346**, 1467 (2014).
32. Y. G. Zhang, M. Pagani, Z. Liu, *Science* **344**, 84–87 (2014).
33. K. T. Lawrence, S. C. Woodard, *Paleoceanography* **32**, 318–324 (2017).
34. N. Meinicke, M. A. Reimi, A. C. Ravelo, A. N. Meckler, *Paleoceanogr. Paleoclimatol.* **36**, e2020PA004115 (2021).
35. E. L. McClymont *et al*., *Clim. Past* **16**, 1599–1615 (2020).
36. H. Dowsett *et al*., *Clim. Past* **12**, 1519–1538 (2016).
37. M. A. Martínez-Botí *et al*., *Nature* **518**, 49–54 (2015).
38. A. M. Barth, P. U. Clark, N. S. Bill, F. He, N. G. Pisias, *Clim. Past* **14**, 2071–2087 (2018).
39. K. E. Kohfeld, Z. Chase, *Earth Planet. Sci. Lett.* **472**, 206–215 (2017).
40. J. E. Tierney *et al*., *Nature* **584**, 569–573 (2020).
41. A. Paul, S. Mulitza, R. Stein, M. Werner, *Clim. Past* **17**, 805–824 (2021).
42. MARGO Project Members, *Nat. Geosci.* **2**, 127–132 (2009).
43. A. C. Mix, A. E. Morey, N. G. Pisias, S. W. Hostetler, *Paleoceanography* **14**, 350–359 (1999).
44. J. D. Annan, J. C. Hargreaves, T. Mauritsen, *Clim. Past* **18**, 1883–1896 (2022).
45. R. A. Rohde, Z. Hausfather, *Earth Syst. Sci. Data* **12**, 3469–3479 (2020).
46. Z. Liu *et al*., *Science* **325**, 310–314 (2009).
47. C. He *et al*., *Sci. Adv.* **7**, eabe2611 (2021).
48. C. W. Snyder, *Nature* **538**, 226–228 (2016).
49. A. M. Haywood *et al*., *Clim. Past* **16**, 2095–2123 (2020).
50. J. D. Shakun, *Quat. Sci. Rev.* **165**, 25–30 (2017).
51. L. B. Stap, P. Köhler, G. Lohmann, *Earth Syst. Dyn.* **10**, 333–345 (2019).
52. L. B. Stap *et al*., *Paleoceanogr. Paleoclimatol.* **33**, 381–394 (2018).
53. J. Hansen, M. Sato, G. Russell, P. Kharecha, *Philos. Trans. A Math. Phys. Eng. Sci.* **371**, 20120294 (2013).
54. B. Bereiter, S. Shackleton, D. Baggenstos, K. Kawamura, J. Severinghaus, *Nature* **553**, 39–44 (2018).
55. P. R. Liautaud, D. A. Hodell, P. J. Huybers, *Earth Planet. Sci. Lett.* **536**, 116137 (2020).
56. A. J. Broccoli, S. Manabe, *Clim. Dyn.* **1**, 87–99 (1987).
57. H. L. Ford, A. C. Ravelo, P. S. Dekens, J. P. LaRiviere, M. W. Wara, *Geophys. Res. Lett.* **42**, 4878–4887 (2015).
58. C. M. Brierley *et al*., *Science* **323**, 1714–1718 (2009).
59. C. Buizert *et al*., *Science* **372**, 1097–1101 (2021).
60. E. W. Wolff, H. Fischer, T. van Ommen, D. A. Hodell, *Clim. Past* **18**, 1563–1577 (2022).
61. T. D. Herbert *et al*., *Science* **377**, 116–119 (2022).
62. A. N. Meckler *et al*., *Science* **377**, 86–90 (2022).
63. Y. Park *et al*., *Proc. Natl. Acad. Sci. U.S.A.* **117**, 25319–25326 (2020).
64. P. Köhler, *Paleoceanogr. Paleoclimatol.* **38**, e2022PA004439 (2023).
65. R. D. Müller *et al*., *Nature* **605**, 629–639 (2022).
66. G. Bayon *et al*., *Sci. Adv.* **9**, eadf3141 (2023).
67. J. W. B. Rae *et al*., *Annu. Rev. Earth Planet. Sci.* **49**, 609–641 (2021).
68. P. Köhler, R. Bintanja, *Clim. Past* **4**, 311–332 (2008).
69. T. B. Chalk *et al*., *Proc. Natl. Acad. Sci. U.S.A.* **114**, 13114–13119 (2017).
70. J. E. Weiffenbach *et al*., *Clim. Past Discuss.*, doi.org/10.5194/cp-2023-83 (2023).
71. S. I. Shin, Z. G. Liu, B. L. Otto-Bliesner, J. E. Kutzbach, S. J. Vavrus, *Geophys. Res. Lett.* **30**, 2002GL015513 (2003).
72. R. Ferrari *et al*., *Proc. Natl. Acad. Sci. U.S.A.* **111**, 8753–8758 (2014).
73. A. J. Watson, G. K. Vallis, M. Nikurashin, *Nat. Geosci.* **8**, 861–864 (2015).
74. M. F. Jansen, *Proc. Natl. Acad. Sci. U.S.A.* **114**, 45–50 (2017).
75. A. Marzocchi, M. F. Jansen, *Nat. Geosci.* **12**, 1001–1005 (2019).
76. A. Martínez-Garcia *et al*., *Nature* **476**, 312–315 (2011).
77. A. Starr *et al*., *Nature* **589**, 236–241 (2021).
78. A. P. Hasenfratz *et al*., *Science* **363**, 1080–1084 (2019).
79. A. Abe-Ouchi *et al*., *Nature* **500**, 190–193 (2013).
80. D. Pollard, *J. Geophys. Res.* **88**, 7705–7718 (1983).
81. S. Barker, G. Knorr, *Nat. Commun.* **12**, 2273 (2021).
82. H. Cheng *et al*., *Nature* **534**, 640–646 (2016).
83. L. E. Lisiecki, *Paleoceanography* **29**, 71–86 (2014).
84. L. D. Pena, S. L. Goldstein, *Science* **345**, 318–322 (2014).
85. C. H. Lear *et al*., *Geology* **44**, 1035–1038 (2016).
86. S. M. Sosdian, Y. Rosenthal, J. R. Toggweiler, *Paleoceanogr. Paleoclimatol.* **33**, 546–562 (2018).
87. J. R. Farmer *et al*., *Nat. Geosci.* **12**, 355–360 (2019).
88. Z. Liu, H. Yang, *Geophys. Res. Lett.* **30**, 2002GL016492 (2003).
89. J. Da, Y. G. Zhang, G. Li, X. Meng, J. Ji, *Nat. Commun.* **10**, 4342 (2019).
90. M. Yamamoto *et al*., *Nat. Geosci.* **15**, 307–313 (2022).
91. Y. Yan *et al*., *Nature* **574**, 663–666 (2019).
92. B. Bereiter *et al*., *Geophys. Res. Lett.* **42**, 542–549 (2015).
93. R. Uemura *et al*., *Nat. Commun.* **9**, 961 (2018).
94. D. C. Lang *et al*., *Nat. Geosci.* **9**, 375–379 (2016).

ACKNOWLEDGMENTS

We thank the reviewers for their helpful comments, the paleoclimate and paleoceanographic communities for making their datasets widely available, the National Centers for Environmental Information of NOAA and the World Data Center PANGAEA for archiving data, and C. Brierley and J. Tindall for providing climate model data. This publication contributed to Beyond EPICA, a project of the European Union's Horizon 2020 Research and Innovation Program (Oldest Ice Core). This is Beyond EPICA publication number 35. **Funding:** This work was supported by the National Science Foundation (grant OPP-2103032 to P.U.C. and grant OCE-1834208 to Y.R.) and the University of Oregon Fund for Faculty Excellence (P.J.B.). **Author contributions:** Conceptualization: P.U.C., J.D.S.; Investigation: P.U.C., J.D.S., Y.R., P.K., P.J.B.; Methodology: J.D.S., Y.R., P.U.C., P.J.B., P.K.; Writing – original draft: P.U.C., J.D.S.; Writing – review and editing: P.U.C., J.D.S., Y.R., P.K., P.J.B. **Competing interests:** The authors declare no competing interests. **Data and materials availability:** In addition to new data developed as part of this study, we used published data from ~130 sources listed in table S1. Source data for Fig. 1 and fig. S13 are provided in the supplementary materials.

SUPPLEMENTARY MATERIALS

science.org/doi/10.1126/science.adi1908
Materials and Methods
Figs. S1 to S17
Tables S1 and S2
References (*95*–*225*)
Supplementary Data S1 and S2

Submitted 9 April 2023; accepted 16 January 2024
10.1126/science.adi1908